JOURNAL OF APPLIED CRYSTALLOGRAPHY

ISSN 1600-5767

Evolution of the pore structure during the early stages of the alkali-activation reaction: an *in situ* small-angle neutron scattering investigation

Claire E. White,[a]* Daniel P. Olds,[b]‡ Monika Hartl,[b]§ Rex P. Hjelm[b] and Katharine Page[b]‡

[a]Department of Civil and Environmental Engineering and Andlinger Center for Energy and the Environment, Princeton University, Princeton, USA, and [b]Lujan Neutron Scattering Center, Los Alamos National Laboratory, Los Alamos, USA. *Correspondence e-mail: whitece@princeton.edu

Received 9 March 2016
Accepted 15 November 2016

Edited by D. I. Svergun, European Molecular Biology Laboratory, Hamburg, Germany

‡ Present address: Spallation Neutron Source, Oak Ridge National Laboratory, Oak Ridge, USA.
§ Present address: European Spallation Source, Lund, Sweden.

Keywords: small-angle neutron scattering; alkali-activated materials; pore structure; gel pores; nanoscale morphology.

Supporting information: this article has supporting information at journals.iucr.org/j

The long-term durability of cement-based materials is influenced by the pore structure and associated permeability at the sub-micrometre length scale. With the emergence of new types of sustainable cements in recent decades, there is a pressing need to be able to predict the durability of these new materials, and therefore nondestructive experimental techniques capable of characterizing the evolution of the pore structure are increasingly crucial for investigating cement durability. Here, small-angle neutron scattering is used to analyze the evolution of the pore structure in alkali-activated materials over the initial 24 h of reaction in order to assess the characteristic pore sizes that emerge during these short time scales. By using a unified fitting approach for data modeling, information on the pore size and surface roughness is obtained for a variety of precursor chemistries and morphologies (metakaolin- and slag-based pastes). Furthermore, the impact of activator chemistry is elucidated *via* the analysis of pastes synthesized using hydroxide- and silicate-based activators. It is found that the main aspect influencing the size of pores that are accessible using small-angle neutron scattering analysis (approximately 10–500 Å in diameter) is the availability of free silica in the activating solution, which leads to a more refined pore structure with smaller average pore size. Moreover, as the reaction progresses the gel pores visible using this scattering technique are seen to increase in size.

1. Introduction

Alkali-activated concrete has emerged over the few past decades as a viable alternative to traditional ordinary Portland cement (OPC)-based concrete because of the proven savings in CO_2 emissions (up to 80–90% reduction) (Duxson, Provis *et al.*, 2007) and comparable mechanical performance (Shi *et al.*, 2006; van Deventer *et al.*, 2012). This type of low-CO_2 concrete utilizes industrial waste materials as the aluminosilicate precursors, such as coal-derived fly ash and ground granulated blast-furnace slag (denoted as slag), which, when mixed with highly alkaline activators (such as a sodium silicate solution), form mechanically hard gel binders (Fernández-Jiménez & Palomo, 2007; Fernández-Jiménez *et al.*, 2006; Palomo *et al.*, 2005; Shi *et al.*, 2006; Steveson & Sagoe-Crentsil, 2005). Metakaolin (formed *via* calcination of kaolinite, a layered aluminosilicate mineral) is also used as an alkali-activated material (AAM) precursor, mainly for the synthesis of low-temperature ceramics (Bell *et al.*, 2009*a*,*b*) and fire-resistant coatings (Temuujin *et al.*, 2011). Furthermore, metakaolin has been useful in elucidating the atomic and nanoscale chemistry occurring during the alkali-activation reaction (White *et al.*,

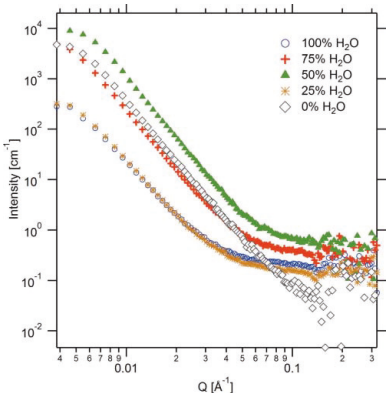

2011) since slag and fly ash are highly heterogeneous materials, even at the nanometre length scale (Duxson & Provis, 2008), which makes it extremely difficult to pinpoint the exact structural mechanisms occurring during the alkali-activation reaction. Nevertheless, precursor particle morphology plays an important role in the alkali-activation reaction process, and therefore there are inherent differences in the structural mechanisms occurring in metakaolin-based and fly-ash-based alkali-activated systems (Lloyd *et al.*, 2009*b*; White *et al.*, 2012), which must be taken into account when using metakaolin as a model system for studying the alkali-activation reaction.

In recent years there has been a significant increase in the number of studies that focus on the atomic structure of AAMs and associated changes that occur during the alkali-activation reaction. Key experimental techniques used to study the atomic structure of alkali-activated pastes include total scattering (in the form of pair distribution function, PDF, analysis) (Bell, Sarin, Driemeyer *et al.*, 2008; Bell, Sarin, Provis *et al.*, 2008; Meral *et al.*, 2011; White, 2012; White *et al.*, 2011; White, Provis, Proffen & van Deventer, 2010), vibrational spectroscopy (Duxson, Lukey & van Deventer, 2007; Rees *et al.*, 2007*a*,*b*; Zhang *et al.*, 2012) and nuclear magnetic resonance (Duxson, Provis, Lukey, Separovic & van Deventer, 2005; Duxson, Provis *et al.*, 2006; Rahier *et al.*, 2007; Singh, Bastow & Trigg, 2005; Singh, Trigg *et al.*, 2005). Furthermore, scanning electron microscopy (SEM) has been used extensively for the characterization of precursor particle morphology and gel formation at the micrometre level (Chen-Tan *et al.*, 2009; Duxson, Lukey & van Deventer, 2006; Fernández-Jiménez *et al.*, 2005; Lloyd *et al.*, 2009*a*,*b*; Williams *et al.*, 2011). However, there are important nanoscale morphological details regarding the alkali-activation reaction and subsequent formation of the gel, which are not accessible using local structure tools (such as PDF analysis) and microstructure analysis techniques including SEM. Transmission electron microscopy (TEM) has been shown to be capable of probing the nanoscale morphology of cured alkali-activated gel pastes (Bell *et al.*, 2009*a*; Blackford *et al.*, 2007; Maitland *et al.*, 2011). However, because of sample preparation requirements and potential beam damage, this technique is currently not suitable for studying the nanoscale morphology changes occurring during the alkali-activation reaction.

There are a range of important details encapsulated in the nanoscale morphology as the alkali-activation reaction progresses, including the evolution of the gel binder morphology. However, the nanoscale pore structure is arguably the most important component controlling long-term durability, since previous investigations have revealed that the intrinsic permeability of OPC-based pastes is controlled by the gel pores (∼20–50 Å) (Scherer, 2012; Scherer *et al.*, 2007). Techniques that are capable of determining the pore size distribution in cements and related materials include nitrogen sorption and mercury intrusion porosimetry. Unfortunately, owing to the need for aggressive pretreatment in the form of drying, these techniques are destructive in nature and can cause severe damage to the pore structure. Hence, the measured pore size distribution tends not to be a true reflection of the actual pore size distribution present in the material (Scherer *et al.*, 2007).

As is the case for conventional OPC-based pastes, AAMs are known to consist of a distribution of pore sizes, ranging from gel pores (∼20–50 Å in diameter) to capillary pores (∼50–500 Å or larger). Furthermore, air voids can be present in the paste and tend to be situated at the micrometre length scale. The long-term durability of conventional cements and AAMs is intimately linked to the percolating pore network of the paste (Scherer, 2012; Scherer *et al.*, 2007), which is affected by precursor selection and activator chemistry for the case of alkali-activated systems. Therefore, small-angle neutron scattering (SANS) analysis is ideally suited for studying the small gel pores controlling permeability in alkali-activated pastes without the need to perform potentially damaging drying-based pretreatments of the samples as is the case for nitrogen sorption and mercury intrusion porosimetry.

Small-angle scattering (SAS), which uses X-ray or neutron radiation to probe the nanoscale morphology of materials, is highly suited for studying in a nondestructive manner the alkali-activation reaction and associated changes occurring at the nanometre length scale. SANS and ultra-small-angle neutron scattering have been used to investigate the pore surface properties of mixed alkali-activated systems (Phair *et al.*, 2003) and metakaolin-based alkali-activated pastes (Maitland *et al.*, 2011; Steins *et al.*, 2012, 2014). These studies revealed that the scattering from the solid, open-pore and closed-pore phases contributed to the SANS data, and that all three phases are present over similar length scales, as they contribute to the scattering over similar Q domains (magnitude of the scattering vector). Furthermore, Maitland *et al.* (2011) concluded from contrast variation experiments that in a sodium-based silicate-activated metakaolin paste the SANS data are dominated by scattering from the pore system. These conclusions were reached on the basis of samples that were previously dehydrated and then soaked in various H_2O/D_2O solutions, with the contrast variation plot revealing the presence of a single minimum.

Steins *et al.* (2012) used *in situ* small-angle X-ray scattering (SAXS) to investigate the nanostructural morphology changes occurring during the alkali-activation reaction for metakaolin-based systems, elucidating the average size of the oligomeric species in solution and how this changed as the reaction progressed for different alkali cations (Na^+, K^+ and Cs^+). However, given that the amorphous alkali-activated paste is reported to consist of roughly 50 Å-sized particles surrounded by a secondary continuous phase or regions of nanoporosity, or a mixture of the two (Gordon *et al.*, 2005), nanoporosity morphology information should also be present in the SAS data. The sensitivity of SAS to nanosized features depends on the particle and void homogeneity in size and shape, and the relative contrast scattering length density of the continuous maxtrix (see below). In particular if the nanosized particle inclusions have the same scattering length density as the continuous phase region surrounding the nanosized particles, then these features will be insensitive to the SAS technique.

As explained below, an advantage of SANS is the ability to use contrast variation to highlight certain features, for example, pores or various components of the solid that differ in scattering length density, as will be carried out in this investigation.

Here, *in situ* SANS is used to characterize the nanoscale morphology of metakaolin- and slag-based pastes and the changes occurring during the alkali-activation reaction over the initial 24 h of formation. Since our previous nanoscale simulations have reported the importance of free silica in the activator for the development of a dense nanostructural morphology (White *et al.*, 2012), our aim for this study is to assess the effect of free silica on the nanoscale morphology gel evolution for metakaolin- and slag-based systems. Contrast variation is used to unequivocally determine that pores make the major contribution to the observed scattering. Here we determine pore size and surface roughness information for each alkali-activated system, together with the changes occurring during the reaction.

2. Materials and methods

2.1. Alkali-activated paste compositions

The alkali-activated pastes studied in this investigation were synthesized from high-purity metakaolin (amorphous layered aluminosilicate), characterized in our previous studies (White *et al.*, 2010*a*,*b*) and ground granulated blast-furnace slag [denoted slag, amorphous glassy calcium aluminosilicate, refer to the article by Lloyd *et al.* (2009*a*) for further details]. The metakaolin precursor was activated with three sodium-based alkaline solutions: a hydroxide-activated ('H-activated') system using NaOH pellets (Sigma–Aldrich), and hydroxide/silicate-activated ('H/S-activated') and silicate-activated ('S-activated') systems using NaOH pellets (Sigma–Aldrich) and amorphous fumed silica (200 $m^2\,g^{-1}$, Aerosil). The slag precursor was activated with two sodium-based alkaline solutions: a hydroxide-activated ('H-activated') system using NaOH pellets (Sigma–Aldrich) and a silicate-activated ('S-activated') system using anhydrous sodium metasilicate (Na_2SiO_3) powder (Sigma–Aldrich). For preparation of each solution, the NaOH/Na_2SiO_3 was dissolved in liquid D_2O (99.9%, Sigma–Aldrich) and then the fumed silica was added (for the H/S- and S-activated metakaolin samples). The solutions were sealed in airtight containers and allowed to equilibrate for at least 24 h whilst being stirred at ~333 K. The alkali-activated paste compositions are given in Table 1. For the metakaolin-activating solutions, the Na_2O dose was 28.0 wt% (*i.e.* 28 g Na_2O per 100 g solid aluminosilicate precursor), and for the metakaolin H/S-activator and S-activator the SiO_2 dose was 27.2 and 54.3 wt%, respectively. For the slag activating solutions, the Na_2O dose was 11.0 wt%, and for slag S-activator the SiO_2 dose was 10.7 wt%. The use of a high water/precursor ratio (1.0 for a mass ratio of D_2O/precursor, 0.9 if using H_2O) for the metakaolin-based pastes is due to the high water demand of metakaolin, and the ratio was selected on the basis of previous investigations of metakaolin-based pastes (Bell, Sarin, Dreimeyer *et al.*, 2008; Provis & van Deventer, 2007; White, Provis, Proffen & van Deventer, 2010). The water/precursor ratio for the slag systems was reduced to 0.39 (for D_2O/precursor) to account for the lower water demand in the presence of slag (Lloyd *et al.*, 2009*b*). D_2O has been used instead of H_2O (or a mixture of D_2O and H_2O as determined by the contrast variation measurements outlined below), as the incoherent neutron scattering background from deuterium is significantly less than that from hydrogen.

Table 1
Alkali-activated paste compositions (oxide molar ratios) studied using *in situ* small-angle neutron scattering analysis.

The stoichiometry of metakaolin is $Al_2O_3{\cdot}2SiO_2$ and that of slag is approximately $Al_2O_3{\cdot}3.96SiO_2{\cdot}5.45CaO{\cdot}0.84MgO$.

Sample name	Na_2O	Al_2O_3	SiO_2	CaO	MgO	D_2O
H-activated metakaolin	1.00	1.00	2.00	0.00	0.00	11.00
H/S-activated metakaolin	1.00	1.00	3.00	0.00	0.00	11.00
S-activated metakaolin	1.00	1.00	4.00	0.00	0.00	11.00
H-activated slag	1.21	1.00	3.96	5.45	0.84	13.21
S-activated slag	1.21	1.00	5.17	5.45	0.84	13.21

2.2. Helium pycnometry

Helium pycnometry was used to obtain the skeletal density of the precursors, metakaolin and slag. Prior to loading in the instrument, the powders were dried at 378 K for 48 h to remove any adsorbed water. For each powder approximately 0.8 g of sample was loaded into the instrument (AccuPyc 1330, Micromeritics, Norcross, GA, USA). The average skeletal density reported by the instrument was used in the calculation of the neutron scattering length density (SLD).

2.3. Nitrogen sorption

Nitrogen sorption was used to determine the nanoscale pore size distribution in S-activated slag paste. Prior to analysis, 2 g of paste was soaked in isopropanol alcohol for 24 h and then dried in a vacuum oven for 24 h at 313 K (until the mass stabilized). The nitrogen sorption measurement was conducted using a Micromeritics ASAP 2010 instrument (Norcross, GA, USA). The sample was subjected to degassing in the instrument at 333 K. The incremental pore volume was obtained using the BJH method (Barrett–Joyner–Halenda) and the adsorption branch of the isotherm.

2.4. Small-angle neutron scattering measurements

SANS measurements were performed using the Low-Q Diffractometer (LQD) at the Lujan Neutron Scattering Center, Los Alamos National Laboratory. The length scale range accessible to LQD is from less than 10 to 1000 Å (Q range of ~0.005–0.3 $Å^{-1}$). The scattering data were reduced to the differential scattering cross section per unit volume, $I(Q)$ (cm^{-1}), as a function of the magnitude of the scattering vector Q ($Å^{-1}$), $Q = (4\pi \sin\theta)/\lambda$, using standard data reduction methods for time-of-flight low-Q data (Hjelm, 1988; Seeger &

Hjelm, 1991). Here λ is the incident neutron wavelength and θ is half the scattering angle.

For the *in situ* alkali-activation measurements the solid aluminosilicate precursors were mixed with the activating D_2O solutions for approximately 30 s by hand (5 g in total, until reaching a uniform fluid consistency) immediately prior to loading between two quartz windows in a specialized 'gel' cell with a 1.5 mm thickness defined by a Teflon spacer. Data collection commenced approximately 15 min after the start of mixing for each sample (the exact time from mixing to measuring was recorded). Each sample was measured for up to 24 h, with 1 h-long measurements acquired approximately every 2 h, since two samples were mounted in the sample changer and scanned alternately. The time reported is the mid-point for each data set (*i.e.* for a data set acquired from 15–75 min after mixing, the time reported is 45 min). Fully cured samples (after 90 d, in powder form) for H- and S-activated metakaolin and S-activated slag were also measured to provide an estimate of the end-point of reaction for these samples.

2.5. Contrast variation

The measured intensity in a SANS experiment is proportional to the variance of fluctuations in scattering length density (SLD), $\overline{\Delta\rho^2}$, in the sample, where $\rho(r)$ is the value of scattering length density with position, r. For a two-phase system, $\Delta\rho = \rho_1 - \rho_2$, where $\rho(r)$ is a function of local chemical composition and density, $\rho(r) = \sum b_i/V$. Here b_i are the nuclear scattering lengths in a sample volume element, V. The b_i values are element and isotope specific; thus, knowledge of $\rho(r)$ gives information about the chemical composition and density, although one must be known (chemical composition or density) in order to extract information on the other.

In the two-phase approximation the SANS SLD of each can be discerned by changing the SLD of one of the phases (Mang *et al.*, 2008). Substitution of deuterium for hydrogen differentially in one of the phases with respect to the other, which is denoted as contrast variation, is used to determine the contrast match condition, the point where the scattering is minimized. By knowing which phase contains the deuterium, and at what concentration, the phase SLD is readily provided for the SANS contrast match condition. This approach is extremely useful in discriminating the SANS contributions from voids and pores, as opposed to other features in complex materials.

Contrast variation was performed on the precursor powders metakaolin and slag, using a five-point contrast curve obtained for a Q value of 0.0046 Å^{-1}. The sample powder was mixed (shaken) with solutions containing different proportions of H_2O to D_2O (100, 75, 50, 25 and 0% H_2O), in a quartz cuvette. 1 mm path length cuvettes were used for samples with 100% H_2O, 75% H_2O/25% D_2O and 50% H_2O/50% D_2O by volume to ensure multiple scattering was not contributing strongly to the scattering profile. 2 mm path length cuvettes were used for samples with higher D_2O content. Each sample was measured for 1 h.

2.6. SANS data interpretation – unified fit model

The Beaucage (1995) unified fit model provides an interpretation of SAS data as resulting from a hierarchical structure. The model envisages that at the largest Q, corresponding to the smallest length scales, $I(Q)$ is dominated by scattering from a basic structure of particles or voids. This domain consists of a visible knee, the Guinier region, giving the size of the basic structure and a Porod power law over larger Q from the surface of the basic structure, visible as a linear region in a $\log[I(Q)]$ *versus* $\log(Q)$ plot. If the basic structures are arranged into a specific geometry, then the Guinier region crosses over into a power law domain at lower Q, the slope of which on a log–log plot corresponds to the dimension of the geometry. In principle, the hierarchical structure can extend over many orders of magnitude in Q with the particles forming clusters, with their own Guinier domains and so on.

As outlined by Beaucage (1996), these structural levels are suited for elucidating the underlying hierarchical behavior of mass and surface geometries. Usually, these are described as mass fractals, those displaying power laws less than 3, and surface fractals, those displaying power laws between 3 and 4. The term 'fractal', however, implies self-similarity over a large domain of length scales, which may not be the case. Nevertheless, the usual interpretation that a power law less than 3 corresponds to the dimensionality of the mass distribution is valid within the assumptions of the Beaucage model (see below). Likewise, a power law between 3 and 4 is usually interpreted as being from surface geometry, with a smooth surface giving a value of 4 and values approaching 3 indicating increasing roughness.

The SAS intensity is the sum of scattering from each structural level, i, of the model, formally,

$$I(Q) = \sum_i \left[G_i \exp(-Q^2 R_{g_i}^2/3) + B_i (Q_i)^{-P_i} \right] + \mathrm{Bk}, \qquad (1)$$

$$Q_i = \frac{Q}{\left[\mathrm{erf}(k_i Q R_{g_i}/6^{1/2})\right]^3}. \qquad (2)$$

In equation (1), G is the Guinier prefactor, the SAS cross section of the structural level, and B is the constant prefactor specific to the Q value where $I(Q)$ crosses over to the power law given by the exponent P. In equations (1) and (2), R_g is the radius of gyration of the structural level. Bk is the residual background. k_i is a constant and is set as 1.06. This analysis assumes monodispersed spheroidal scatterers, with each structural level consisting of a single size of scatterers (size obtained by the Guinier law), which leads to an important caveat in interpreting SAS in terms of this model. A lognormal, for example, can lead to power law scattering over the limited Q domain available in the SAS measurement.

It is important to the interpretation of SAS from cementitious materials that the pores are not monodispersed but rather consist of a distribution of sizes ranging from the nanometre to micrometre length scale. This polydistribution of pore sizes can lead to a Porod-like region, without there actually being information from surface roughness scattering.

Therefore a preliminary analysis of the data has been carried out in this study to assess if the data could be fitted using a polydispersity model (see supporting information for details). However, the analysis revealed that the data could not be fitted consistently (as the alkali-activation reaction progressed), and therefore the most appropriate analysis approach is the unified fit method, as implemented in the *Irena* package (Ilavsky & Jemian, 2009; Potton *et al.*, 1988). The suitability of this approach will be discussed below, with specific reference to complementary experimental techniques (nitrogen sorption analysis) on the pore structure of AAMs. Furthermore, the estimated pore size diameters obtained in this investigation are based on the equation for a monodispersed sphere ($R_g^2 = \frac{3}{5}R^2$), and therefore these sizes should be taken as rough estimates. More accurate information on the pore size distribution would be accessible using an analysis approach incorporating polydispersity during conversion of the radius of gyration to pore size (Beaucage *et al.*, 2004; Mazumder & Sequeira, 1992). However, this approach as implemented in the *Irena* package requires the power-law exponent to be 4.0 (note that an exponent of 4.0 is not required in general for polydispersity analysis), which was not the case for the majority of data sets acquired in this investigation. Furthermore, it is important to note that multiple scattering can distort the apparent sphere distribution obtained from analysis of SAS data (Mang & Hjelm, 2013; Mazumder & Sequeira, 1992). However, in this investigation it will be shown that the pore size obtained using the unified fit method is in good agreement with complementary nitrogen sorption data.

In this investigation, the Guinier radius of gyration (R_g) and the power-law exponent (P) are reported for the unified fits containing one or more structural levels associated with the various alkali-activated systems, together with the changes occurring to these fits as the reaction proceeds. From these fits it is possible to assess the characteristic length scales and changes occurring in the nanoscale morphology during the alkali-activation reaction.

3. Results and discussion

3.1. Contrast variation of metakaolin and slag: pores *versus* solids

In the materials of interest here (AAM precursors) the structures are complex and consist of pores and solid inclusions with different chemical compositions and densities. It is important to determine the extent to which each of these features is contributing to the SANS, particularly to the Guinier domains, from which their sizes are determined. Strictly speaking the scattering from a sample with two homogeneous phases will be null at the contrast match point only for $Q = 0$. At this point both phases have the same SLD. This method can be used to distinguish between scattering from pores where $\rho = 0$ and solid inclusions, for which usually $\rho \neq 0$, given the chemical compositions. However, the vignette of the SANS measurement does not access this point without extrapolation using a model, which is not available for these complex multilength-scale materials. As a result we use the lowest Q = 0.0046 Å^{-1} at which there is a reliable measured point to estimate the null point with the understanding that there are residual fluctuations at *ca* 200 Å due to the finite Q and heterogeneity.

In this investigation contrast matching has been performed on the solid precursor powders metakaolin and slag, with the scattering profiles given in Fig. 1. The corresponding contrast variation plot for slag is displayed in Fig. 2. If the two-phase

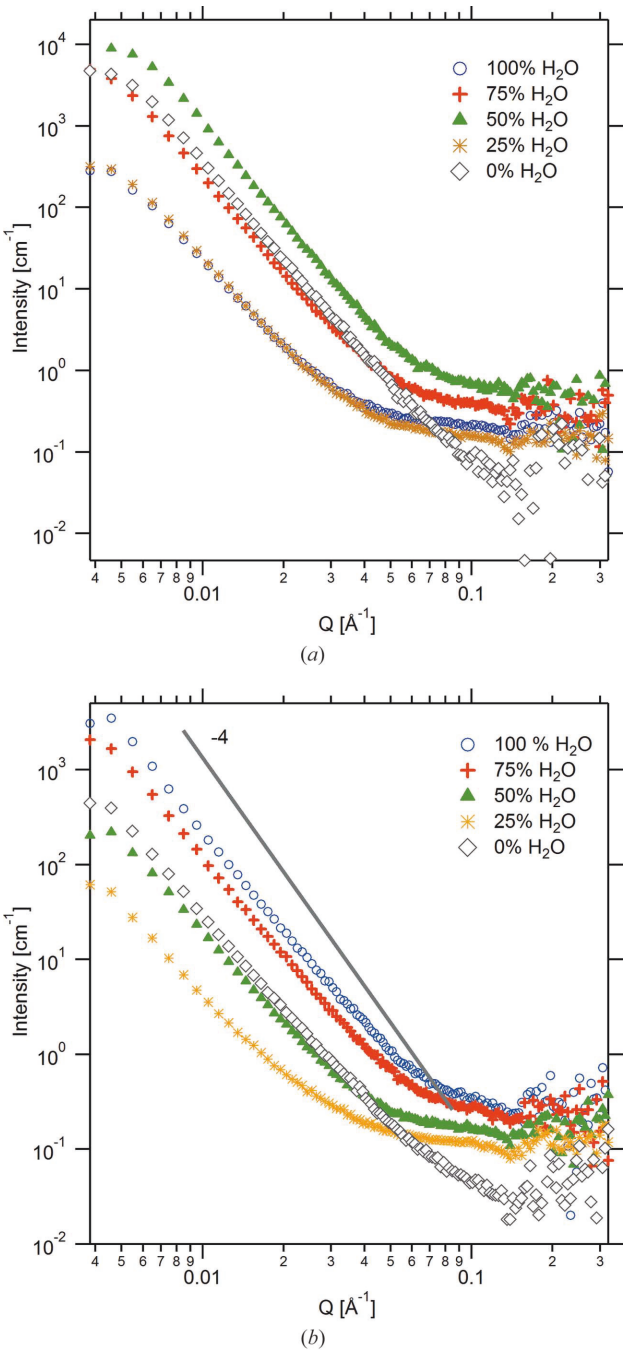

Figure 1
Small-angle neutron scattering profiles for H_2O/D_2O contrast variation of (*a*) metakaolin and (*b*) ground granulated blast-furnace slag. Percentages are given in terms of volume.

approximation holds, namely that this is only one contrast match point, then theory dictates that $I(Q) \propto \Delta\rho^2$ and a plot of $I(Q)$ *versus* ρ is a quadratic (Mang *et al.*, 2008). This expectation was clearly the case for slag but not for metakaolin, where inclusion of different amounts of D_2O in the mixture did not give the expected contrast dependence; there were two distinct minima in the intensity, at 30% and close to 100% H_2O. We speculate that this is due to significant large-length-scale (200 Å) chemical (including isotopic H/D) and/or density heterogeneity, pointing to a limitation of the use of this approximation.

The skeletal density was measuring using helium pycnometry in order to calculate the scattering length density of the precursor powders. For metakaolin the skeletal density was 2.59 g cm^{-3}. With an approximate stoichiometry of $Al_2Si_2O_7$ (if taking into account the residual H/D atom the stoichiometry would be $Al_4Si_4O_{14.5}H$ as determined using thermogravimetric analysis; White *et al.*, 2010*b*), the SLD of metakaolin was calculated to be 3.9×10^{-6} Å^{-2} (with bounds of 3.8×10^{-6} to 4.2×10^{-6} Å^{-2} taking into account the possibility of H or D being present in the structure). This SLD value corresponds to an H_2O/D_2O volume ratio of 36/64%. Hence, given that the rough approximation for the null scattering solution (~30% H_2O) matches the calculated SLD for metakaolin (knowing the stoichiometry and skeletal density), it is likely that the scattering is due to H_2O/D_2O-filled voids existing in between metakaolin particles when the powder is dispersed in H_2O/D_2O.

The contrast variation data for slag is shown in Fig. 2, plotted as $I(Q)^{1/2}$ *versus* solvent SLD. The linear fit is consistent with expectations, where $I(Q)^{1/2} = 0$ gives the contrast point, resulting in an H_2O vol.% of 29, which corresponds to an SLD of 4.4×10^{-6} Å^{-2}. This value is similar to that for an alkali-activated slag paste investigated by Thomas *et al.* (2012), where a contrast point of 20 ± 1 vol.% H_2O or 5×10^{-6} Å^{-2} was obtained. Calculation of the SLD using the known stoichiometry (Table 1) and skeletal density (2.80 g cm^{-3}) of slag results in a value of 3.8×10^{-6} Å^{-2}. The difference between the calculated and experimental results indicates that deuterium is present in the matrix as well. Given that slag is weakly cementitious, meaning that it reacts when immersed in water, it is likely that the SLD of the solid is changing as a function of time and tending towards the SLD of a hydrated slag-based paste. Furthermore, the extent of incorporation of deuterium in the calcium (sodium) aluminosilicate hydrate [C–(N)–A–S–H] gel paste will probably change as the H_2O/D_2O ratios are altered, since it is well known that calcium silicate hydrate (C–S–H) undergoes full H/D exchange when exposed to solutions containing D_2O (Thomas *et al.*, 2012). Another possible reason for the discrepancy between our SANS-derived SLD and the calculated value pertains to the contrast matching method. Ideally the contrast match point is derived from the intensity at $Q = 0$. However, this is experimentally impossible and here a Q value of 0.0046 Å^{-1} was used. Nevertheless, it can be concluded from the contrast matching experiment for slag that the scattering from the slag particles is minimal in an H_2O/D_2O solution containing 29% H_2O, where the SLD for this solution roughly matches the calculated SLD of slag taking into account the chemical formula and skeletal density. Therefore, the pores dominate the scattering seen in the SANS data away from the contrast match point.

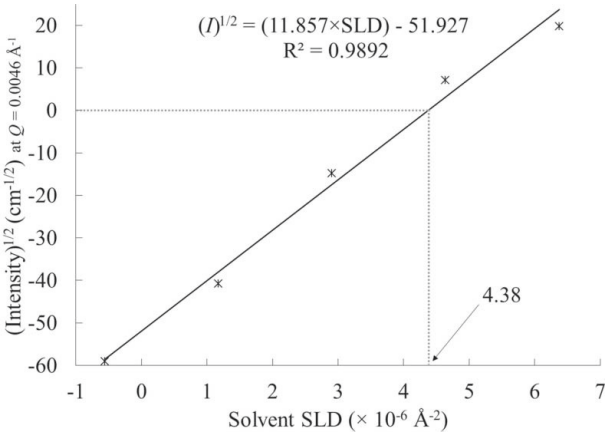

Figure 2
Contrast matching plot of ground granulated blast-furnace slag calculated at a Q value of 0.0046 Å^{-1}. The line is obtained using a linear function.

3.2. Unified fit analysis of metakaolin and slag

In order to assess pore surface scattering (roughness) in the precursor powders, Porod parameters were extracted from the SANS data of metakaolin and slag using the unified fit method outlined in the *Materials and methods* section. Attempts to extract an average size using the Guinier approximation over the low-Q SANS proved futile, as the R_g values that resulted from the fits over the accessible low-Q domain did not meet

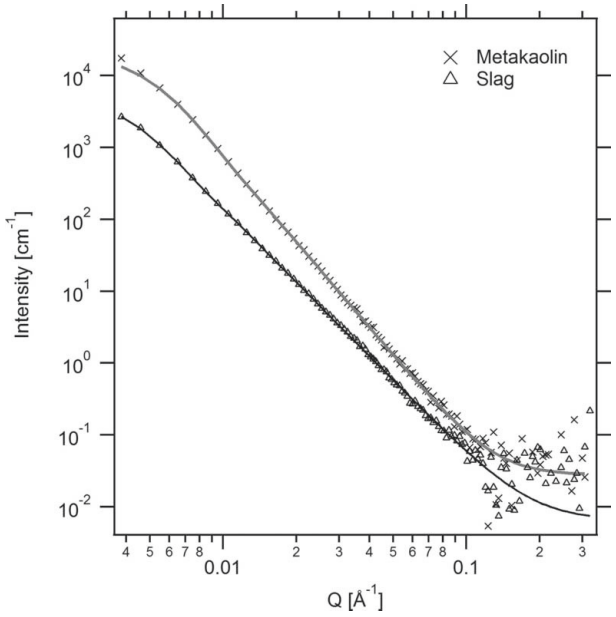

Figure 3
Small-angle neutron scattering patterns of metakaolin and slag precursor powders, and their corresponding unified fits (using a one-structural-level approach, results given in Table 2). The experimental data error bars are excluded for clarity but are comparable to those seen in Fig. 9.

Table 2
Unified fit results of metakaolin and slag, including the error associated with the fits.

Precursor	R_g (Å)†	Porod slope
Metakaolin	381 ± 19	3.96 ± 0.04
Slag	461 ± 98	3.43 ± 0.05

† Values for the radius of gyration are rough estimates, as explained in the text.

the requirement for the Guinier approximation that $QR_g < 1.3$. Therefore, we report the values here as fitting parameters and as coarse estimates of R_g. The fits are displayed in Fig. 3 with the associated fit parameters given in Table 2. The fits reveal that the SANS from these two precursors consists of surface scattering (Porod regions where the slope is between 3 and 4): for metakaolin $P = 3.96 \pm 0.04$, for slag $P = 3.43 \pm 0.05$. Our interpretation is that the metakaolin surfaces are indistinguishable from smooth (where a smooth surface corresponds to $P = 4$), whereas the surface for slag is rougher. As a result of the smooth surface of metakaolin, the corresponding specific surface area can be calculated and is found to be 9.464×10^{-4} cm^2 cm^{-3} when using an SLD of 3.9×10^{-6} Å^{-2}. For metakaolin the bulk density was calculated to be 0.64 g cm^{-3} (±0.03 g cm^{-3}, as determined during loading of the cuvettes for the contrast variation measurements). This results in a specific surface area value of 14.8 m^2 g^{-1}, which is slightly higher than the corresponding value for the parent kaolinite material (KGa-1b, with a specific surface area of 11.7 m^2 g^{-1} determined using the nitrogen BET method; Pruett & Webb, 1993). The Porod scattering agreed with SAXS data for metakaolin dispersed in water previously observed by Steins *et al.* (2014). The characteristic void size derived from the transition from surface to mass fractal scattering observed in the ultra-small-angle X-ray scattering (USAXS) domain (~0.0005–0.01 Å^{-1}) was not reported for metakaolin in their investigation, although from their data it appears that the knee associated with the Guinier region is located at $Q \simeq 0.01$ Å^{-1}. The SANS data on metakaolin given in Fig. 3 show the characteristic transition into the putative Guinier domain at lower $Q \simeq 0.004$–0.005 Å^{-1}, suggesting a larger void size than observed previously (Table 2).

3.3. *In situ* SANS study of the alkali-activation reaction

SANS patterns from the H-activated, S-activated and H/S-activated metakaolin as a function of reaction time are given in Fig. 4, together with the patterns from dry metakaolin (see the supporting information for all SANS data sets together with the corresponding Porod and Kratky plots). The nanoscale structural evolution observed by SANS during the course of the reaction is different for each of the activation conditions. Fig. 4(*a*) shows the changes in SANS with reaction time for the H-activated metakaolin. However, compared to the scattering from the dry metakaolin precursor and the dry fully cured alkali-activated sample (labeled as 'powder' in Fig. 4), the changes over the initial 23 h of reaction are relatively small. In contrast, the H/S-activated metakaolin (Fig. 4*b*) shows significant changes in the SANS profile during this time frame (up to ~21 h), which are indicative of relatively large changes occurring in the nanoscale morphology; significantly, the low-Q scattering intensity decreases as the reaction proceeds. The S-activated metakaolin reaction (Fig. 4*c*) shows a similar behavior to H-activated metakaolin, where there are even fewer changes in the SANS patterns during the initial stages of reaction. By 90 d for the H- and S-activated metakaolin samples (labeled as 'powder' in Fig. 4) pores are seen to develop at ~0.007 and 0.03 Å^{-1}, respectively. As will be shown later *via* unified fits of the data, these pores are seen to emerge during the alkali-activation reaction, with the pores in H-activated metakaolin being larger in diameter compared to those in S-activated metakaolin.

The SANS data for the dry slag precursor and the H- and S-activated slag pastes during the initial 16 h of reaction are given in Fig. 5, clearly showing that the slag pastes also display significant changes in the nanoscale morphology during the initial stages of reaction, especially for S-activated slag. For H-activated slag, the majority of changes seen during the initial stages of reaction are bounded within a Q range of 0.008–0.05 Å^{-1} ($R_g \simeq$ 20–125 Å). On the other hand, for S-activated slag the SANS data reveal that changes are occurring over the entire measured Q range.

We have calculated the Porod invariant (Q_P) for the lowest-Q structural level (obtained from the unified fits as outlined in the next section) for the metakaolin-based pastes, as displayed in Fig. 6. The invariant is associated with total void volumes [$Q_P = 2\pi^2\Phi(1-\Phi)\Delta\rho^2$, where Φ is the void volume fraction] and is seen to change as a function of time for the various pastes. From this comparison it is evident that the activator plays a crucial role in governing the evolution of the invariant. For H-activated metakaolin the invariant is seen to both decrease and increase during the initial stages of reaction, whereas for H/S- and S-activated metakaolin the invariant is seen to decrease. Furthermore, for metakaolin-based pastes the invariant is seen to behave similarly for all three systems for the first couple of hours, after which there is a significant increase/decrease in the invariant depending on the activator chemistry.

The large change in the invariant after 4 h of reaction correlates with previous investigations on metakaolin-based pastes, where the initial stages of reaction are dominated by aluminium dissolution from the precursor (Provis *et al.*, 2005; White *et al.*, 2012). Only when the local supersaturation of silica and alumina is reached does precipitation of the alkali aluminosilicate gel occur, which has been seen to happen 4 h after initial mixing for S-activated metakaolin using X-ray PDF analysis (White *et al.*, 2013) and rheometry measurements (Steins *et al.*, 2012). For H-activated metakaolin the setting time is much longer, with laboratory synthesis revealing that even after 24 h of curing at room temperature these pastes retain partial fluidity and have not obtained sufficient strength to be demolded. On the other hand S-activated metakaolin pastes have solidified by 24 h. Hence, the increase in the invariant at ~4 h in Fig. 6 for H-activated metakaolin is not associated with the setting time. This agrees

with the X-ray PDF analysis results, which revealed that during the initial 10 h of reaction for H-activated metakaolin (the period of time measured using this technique) the system is most likely dominated by dissolution of the precursor. Note that the X-ray PDF analysis results were obtained using H_2O (White *et al.*, 2013). However, here the SANS experiments were conducted using D_2O, which is known to affect the kinetics of reaction for cementitious materials (Thomas & Jennings, 1999) and, therefore, should be taken into account whenever comparing experimental techniques using H_2O/D_2O.

During the initial aluminium dissolution from metakaolin in the H-activated system, it is likely that the aluminosilicate layers will undergo exfoliation, whereby the individual aluminosilicate layers 'peel apart' (White *et al.*, 2011, 2012). It is possible that this exfoliation commences approximately 4 h after initial mixing, leading to a significant increase in the number of pores (void volume) at a particular length scale and an associated increase in the invariant. On the other hand, for S-activated metakaolin the availability of silica in solution tends to lead to coating of the partially dissolved particles in aluminosilicate gel, which may limit the extent of exfoliation.

Our SANS analysis gives the Porod power law scattering during the initial stages of the alkali-activation reaction (first 24 h) and therefore can determine if there are significant changes occurring in the surface roughness scattering as the reaction proceeds. As seen in Fig. 4(*a*), it is evident that metakaolin displays a power law scattering close to $I(Q) \propto Q^{-4}$ (a one-level unified fit gives a Porod regime of 3.96 ± 0.04). For S-activated metakaolin, analysis of the Porod scattering (results presented in the next section) reveals that the scattering is from the surface and the roughness remains relatively unchanged throughout the course of the reaction ($P \simeq 4$). This result is contrary to the SANS contrast variation measurements by Maitland *et al.* (2011) on well cured S-activated metakaolin-based pastes, where the power law scattering was shown to obey an $I(Q) \propto Q^{-3}$ relationship (Maitland *et al.*, 2011). None of the samples measured by Maitland *et al.* had an $I(Q) \propto Q^{-4}$ dependence. Using a three-phase analysis approach they described the sources of scattering as being from the solid, open pores and closed pores and concluded that the dominant contribution to the SANS patterns was from the pores over the measured Q range

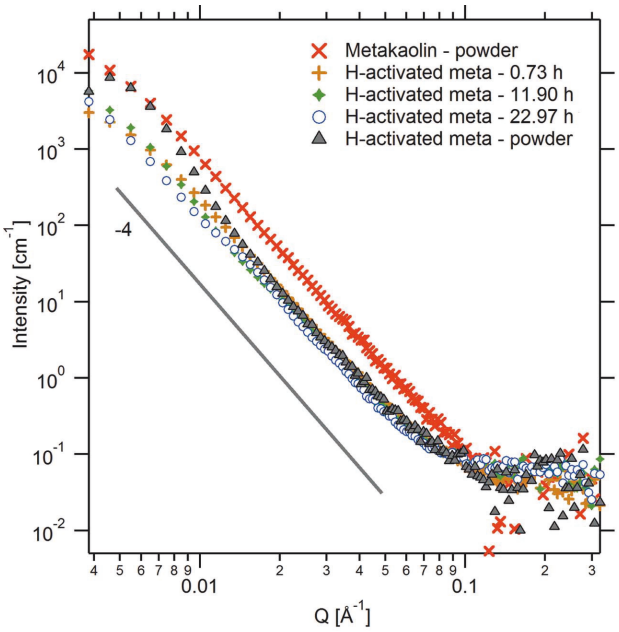

(*a*)

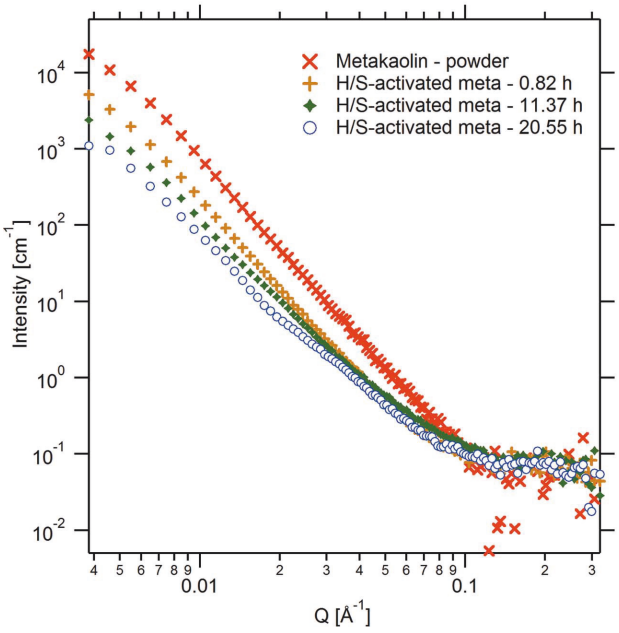

(*b*)

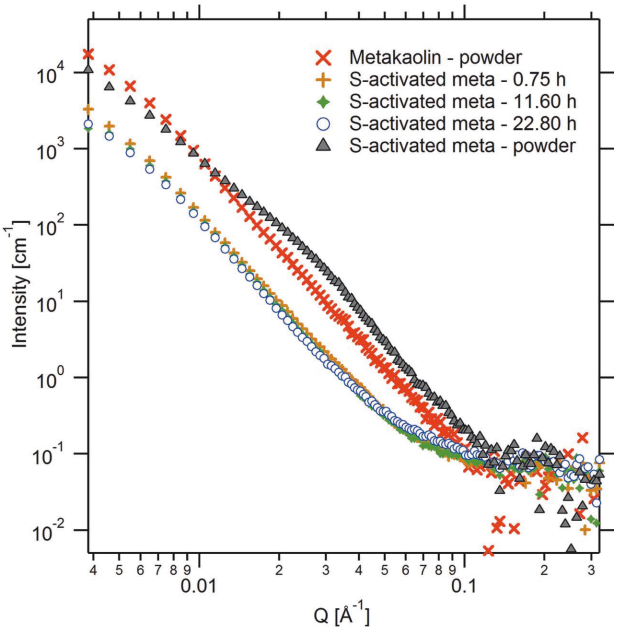

(*c*)

Figure 4
Small-angle neutron scattering pattern of dry metakaolin and selected patterns of the (*a*) H-activated, (*b*) H/S-activated and (*c*) S-activated metakaolin pastes during the alkali-activation reaction. Error bars are excluded for clarity but are comparable to those given in Fig. 9.

(0.023–0.2 Å^{-1}). They attributed the deviation of the power law scattering exponent from −4 to a non-uniform neutron contrast from the pores and possible mass fractal scattering from remnant metakaolin grains. Possible reasons for this discrepancy may include the source of metakaolin and associated properties such as purity and particle morphology. Moreover, any pretreatment of the sample prior to measurement, such as drying [as was the case for Maitland *et al.* (2011)], may alter the pore surfaces and associated power law scattering profile.

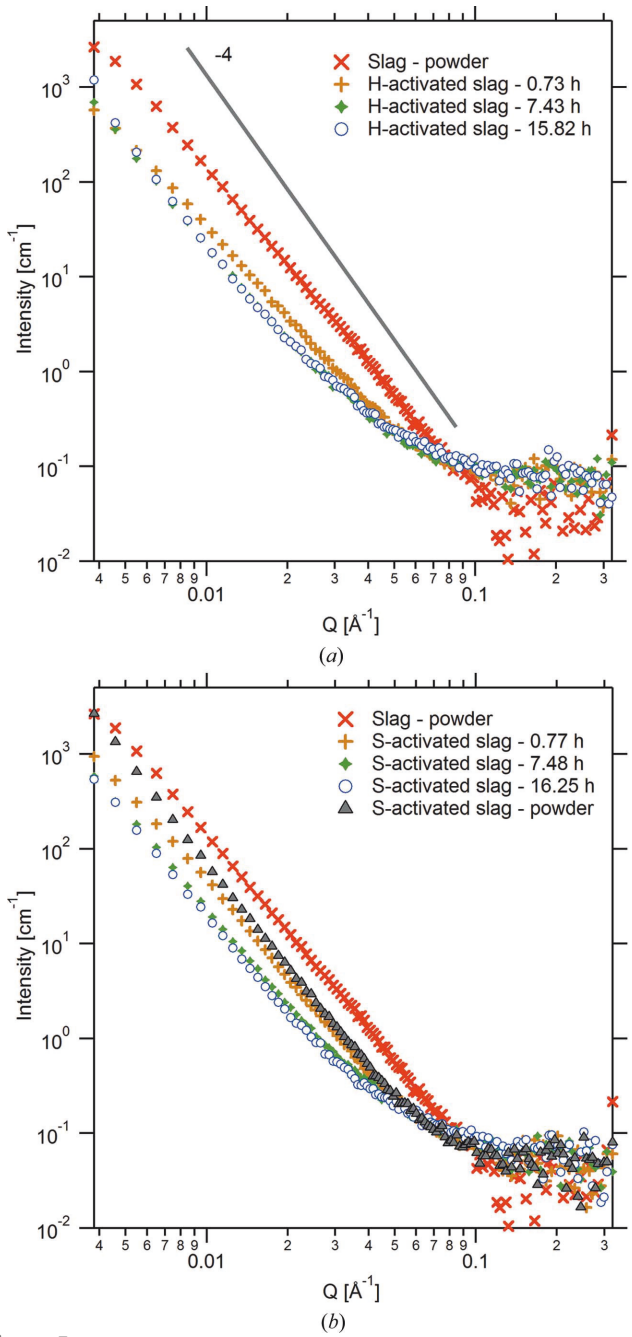

Figure 5
Small-angle neutron scattering pattern of slag and selected patterns of the (*a*) H-activated and (*b*) S-activated slag pastes during the alkali-activation reaction. Error bars are excluded for clarity but are similar to those in Fig. 9.

The slope of the double log plots implies that the scattering is from surface morphologies with sizes that are at the limit of the SANS Q domain. Initially these surfaces are likely to belong to the powder crystallites, transitioning to voids as the sample consolidates as the reaction proceeds. In the case observed here where the larger-scale structures, taken to be D_2O-filled voids (from the outcome of the contrast variation results), have smooth interfaces their contribution to the measured SANS goes as $I(Q) = 2\pi N \Delta\rho^2 S Q^{-4}$, where N is the average number of voids per unit volume and S is the average void surface area. Assuming that the contrast of the voids relative to the matrix ($\Delta\rho$) does not change, then the product NS or equivalently S/V, where V is the average void volume, must become smaller with time [since $I(Q)$ is decreasing in Fig. 6]. This argument implies that the number of voids per unit volume is decreasing, either because they are being consumed or consolidated into larger voids (the intensity decreases as the inverse of the void radius, $I \sim R^{-1}$ in this case) or because the voids are decreasing in size. Therefore, the surfaces that originally existed in the system at the time of initial mixing that contribute to the low-Q scattering intensity are seen to disappear as the reaction progresses owing to the precipitation of gel on the partially dissolved particles. The most likely explanation for the decrease in the invariant (Fig. 6) is that, as the gel precipitates, the product impinges on the pore volume, thereby decreasing the overall size of the pores and reducing the measured intensity at low Q values.

3.4. Unified fit analysis of the alkali-activation reaction

A qualitative assessment of the time-dependent changes in the SANS data resulted in new understanding of the changes that occur during the course of the reaction process. We now turn to analysis using the unified fit method, as outlined in the *Materials and methods* section, to obtain quantitative information on the nanoscale pore size and surface evolution during the alkali-activation reaction. The unified fit method has been applied to the data displayed in Figs. 4 and 5, with the fits to all data given in the supporting information

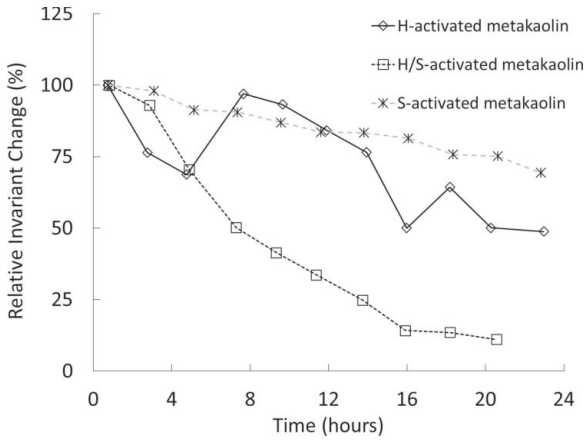

Figure 6
Relative change in the SANS Porod invariant as the alkali-activation reactions progress (for the lowest-Q structural level obtained from the unified fits).

(Figs.S1–S5). The R_g and P [equation (1)] parameters resulting from the fits for the various alkali-activation reactions over the initial 16–24 h of formation, and for the paste (in dry powder form) at 90 d (if available), are presented in Figs. 7 and 8. An example of the agreement between the experimental data set and the fit is shown in Fig. 9, where the data for the dry H-activated metakaolin powder at 90 d have been fitted using a two-level model. The first level is present at low Q values (~0.004–0.01 Å^{-1}) and consists solely of a Guinier region without a power law at lower Q within the vignette of the SANS measurement (no Porod region associated with the low-Q level was needed to adequately fit the scattering profile in Fig. 9). The second level is present at higher Q values and consists of both the Guinier and the Porod regions. For each level (if both the Guinier and the Porod regions are present) the radius of gyration (R_g) and Porod slope are reported, as well as the associated fit error. The Guinier regions in these data reflect changes occurring to the pores in the alkali-activated materials, as determined earlier using contrast variation. Multiple Guinier regions in a single scattering profile indicate that multiple pore systems (at different length scales) exist in the alkali-activated material. Note that the sizes obtained for any Guinier region with a reported R_g greater than 280 Å in this investigation should be treated as a coarse estimate for the

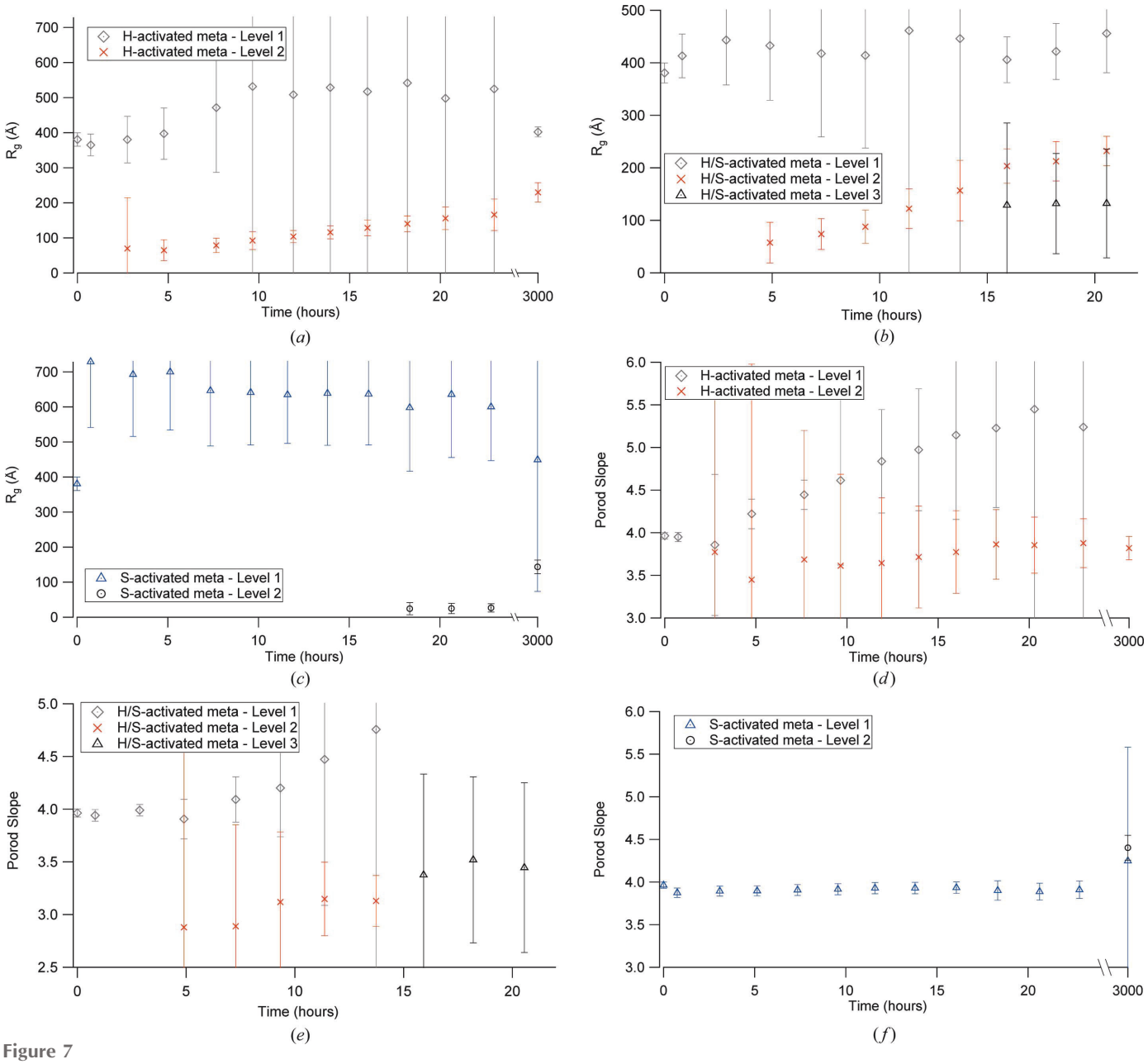

Figure 7
Unified fit parameters (for several structural levels) obtained for the H-activated, H/S-activated and S-activated metakaolin alkali-activation reactions, showing the radius of gyration for the Guinier region for (*a*) H-activated, (*b*) H/S-activated and (*c*) S-activated metakaolin, and the Porod exponent for (*d*) H-activated, (*e*) H/S-activated and (*f*) S-activated metakaolin. The H-activated and S-activated metakaolin paste powder samples (fully cured) are denoted as 3000 h. The precursor metakaolin is given as 0 h.

same reasons stated above. Therefore, levels that consist of Guinier regions with R_g values above ~300 Å are included in Figs. 7 and 8 for completeness, but the R_g values for these levels are not accurate (Level 1 for H-activated metakaolin, Level 1 for H/S-activated metakaolin, Level 1 for S-activated metakaolin, Levels 1 and 2 for H-activated slag, Level 1 for S-activated slag).

The parameters from the unified model fits for the *in situ* reaction of H-activated and S-activated metakaolin are given in Fig. 7, where it is clear that the development of the nanoscale morphology over the initial 24 h of reaction is dependent on the nature of the activator. It is seen for H-activated metakaolin that well defined pores develop ~4 h after initial mixing. These pores are roughly 170 Å in diameter, assuming a spherical morphology (R_g of 65 Å). Hence, these pores can be classified as capillary pores, as opposed to gel pores. The presence of free silica in solution dramatically changes the characteristic pore size found in the Level 2 part of the unified fit, where it is clear that the average pore size is smaller for S-activated metakaolin (Fig. 7*c*). These smaller pores do not develop until ~18 h after initial mixing and are approximately 65 Å in diameter, which is at the upper limit of the size of gel pores found in OPC-based paste (Scherer *et al.*, 2007). The investigation by Steins *et al.* (2014) revealed that the pores present in S-activated metakaolin analyzed by USAXS/SAXS are roughly 20–40 Å in size (radii, modeled as spherical pores) and tend to increase slightly in size as the reaction progresses (over the course of six months). Hence, the pore size determined in our investigation is fairly similar to the size reported for a similar paste at six months, with differences attributable to varying stoichiometry, sample age and data fitting procedure.

Although the errors associated with the pore sizes found in H/S-activated metakaolin are relatively large, the general trend of pore size development is in between that of H- and S-activated metakaolin. The pores emerge ~5 h after mixing and tend to follow the same behavior as the H-activated system (Fig. 7*b*). 16 h after mixing, a second Guinier region emerges in the data for H/S-activated metakaolin, although the accuracy of the refinement is low. This region consists of smaller pores and is in agreement with the trend found in

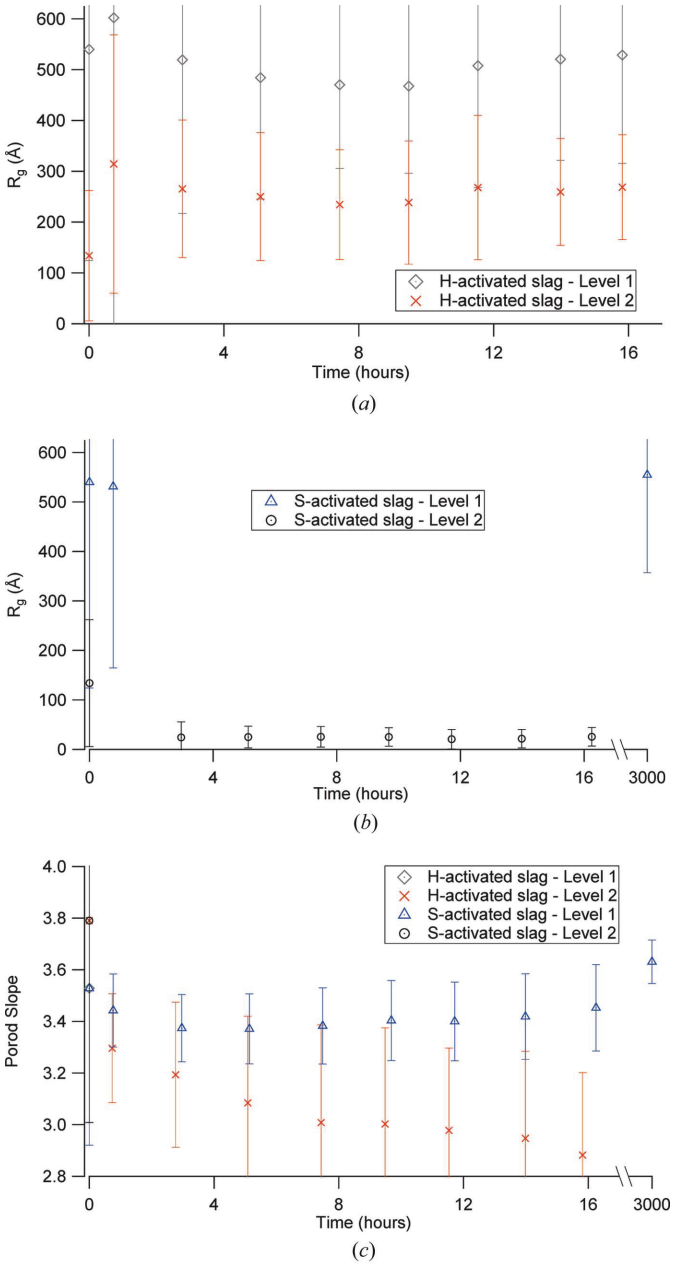

Figure 8
Unified fit parameters (for several structural levels) obtained for the H-activated and S-activated slag reactions, showing (*a*) the radius of gyration for the Guinier region for H-activated slag, (*b*) the radius of gyration for the Guinier region for S-activated slag, and (*c*) the Porod exponent for both H- and S-activated slag. The S-activated slag paste powder sample (fully cured) is denoted as 3000 h. The precursor slag is given as 0 h.

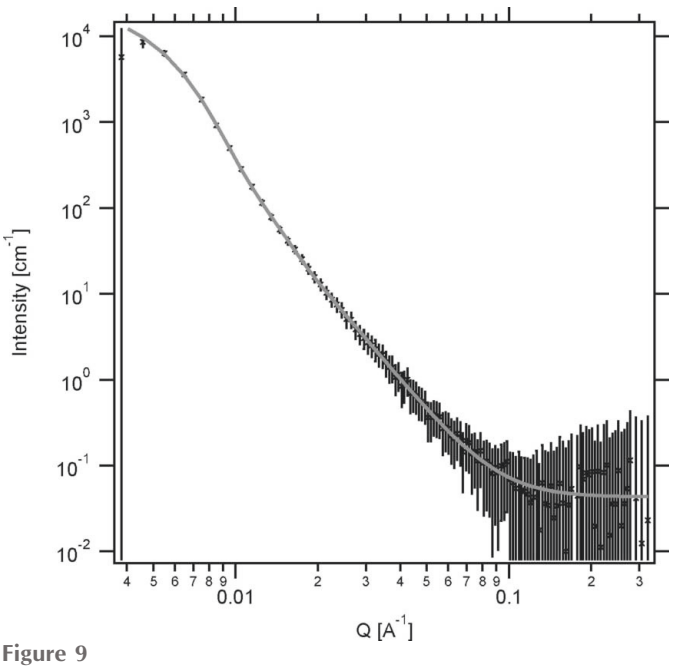

Figure 9
Small-angle neutron scattering pattern of fully cured H-activated metakaolin paste in powder form and the unified fit (using a two-level approach). The experimental data error bars are included.

S-activated metakaolin. Hence, over the course of the initial 20 h the H/S-activated metakaolin paste develops two distinct pore size domains within the length scales accessible using SANS.

As the reaction progresses there are distinct trends in pore size development according to the type of activator used. For H-activated metakaolin the pores increase in size as the reaction progresses. On the other hand, for S-activated metakaolin the pores do not change in size until 24 h after mixing. By 90 d the pores in S-activated metakaolin have increased in size, although they remain smaller than those found in H-activated metakaolin and may have been affected by any exposure to drying conditions. These results show that the type of activator used greatly influences the characteristic size of pores found in the paste, together with the changes in size as the reaction progresses. Although it is already known that the average pore size in H-activated metakaolin is larger than that in S-activated metakaolin (Duxson, Provis, Lukey, Mallicoat *et al.*, 2005), standard laboratory characterization techniques fail to capture the *in situ* changes that occur during the reaction. Furthermore, the pore size cannot be probed in the laboratory using techniques such as nitrogen sorption and mercury intrusion porosimetry until the paste attains sufficient stiffness so that the pore fluid can be removed from the sample. This removal process is known to be capable of inducing changes in the microstructure of the samples, and therefore there is a distinct possibility that the pore sizes obtained using such methods have associated errors (Scherer *et al.*, 2007). One of the main advantages of using a technique such as SANS is that the technique is nondestructive and does not require the samples to have a given stiffness prior to commencement of the measurement, enabling new data on the development of the pore structure during the early stages of reaction to be obtained.

The influence of calcium on the alkali-activation reaction is an area of intense research, because it is known that the inclusion of calcium leads to the formation of phases [such as C–(N)–A–S–H] that are similar to the C–S–H gel found in OPC-based paste (Brough & Atkinson, 2002; Myers *et al.*, 2013; Richardson *et al.*, 1994). The C–S–H gel immobilizes water in (i) the interlayer spacing between the calcium silicate sheets of the gel and (ii) the small gel pores with sizes ranging from 20 to 50 Å (Allen *et al.*, 2007). This immobilization of water in the paste at the nanometre length scale (as opposed to in larger-sized capillary pores) is thought to improve the overall durability of the material owing to a lower permeability that is associated with smaller pore sizes (Scherer *et al.*, 2007). Nevertheless, other important parameters also influence the durability of pastes, including the overall porosity of the material together with the connectivity of the pores (Jennings *et al.*, 2008). In order to obtain a more complete understanding of the influence of the pore size on the durability of AAMs, it is critical that the pore size is accurately characterized. SANS plays a crucial role in this characterization since it can access the smaller-size pores that tend to remain mostly inaccessible using other techniques: apart from nitrogen sorption, which requires aggressive pretreatment of the sample (drying) prior to measurement (Scherer *et al.*, 2007), and therefore may result in a measured pore structure which is different from that existing in the unaltered paste (not subjected to drying).

Fig. 8 displays the characteristic sizes (R_g) obtained for the Guinier components of the fits for slag-based alkali-activated pastes. It is clear that the slag-based pastes follow the same trend as metakaolin in terms of the average pore size for the different activators. For H-activated slag, large pore sizes are indicated by the very low Q turnover in the data (Fig. 5*a*), but the lack of a usable Guinier regime over the lowest Q domain makes the estimate unreliable (Fig. 8*a*). On the other hand, for S-activated slag the average pore size is significant smaller (∼65 Å in diameter), and the appearance of these pores occurs approximately 3 h after initial mixing (Fig. 8*b*). Hence, this difference in characteristic pore size will influence the apparent permeability of the sample, since previous measurements of the diffusivity for OPC-based pastes using beam bending have revealed that the gel pores and small capillary pores control the permeability of liquid through the sample (Valenza & Thomas, 2012).

Comparison of the SANS results in Fig. 8 with porosimetry data obtained using nitrogen sorption (Fig. 10) for an S-activated slag paste at 4 d reveals that the pore size obtained using SANS (∼65 Å) is very similar to that obtained by nitrogen sorption (∼55 Å). Therefore, although there is a slight difference in the values obtained, which may be due to limitations of the unified fit approach, uncertainties inherent in the application of the BET approximation in heterogeneous materials (nitrogen sorption data) (Mang *et al.*, 2000) or the extent of curing (3–16 h for SANS results compared with 4 d for nitrogen sorption), the results show that the unified fit approach is appropriate for analyzing the pore structure of cementitious materials.

As mentioned previously, another important parameter obtained using the unified fit approach is the Porod slope, which provides information on surface geometry (*i.e.* surface roughness). The Porod scattering for the various alkali-activated pastes is illustrated in Figs. 7(*d*)–7(*f*) (H-, H/S- and

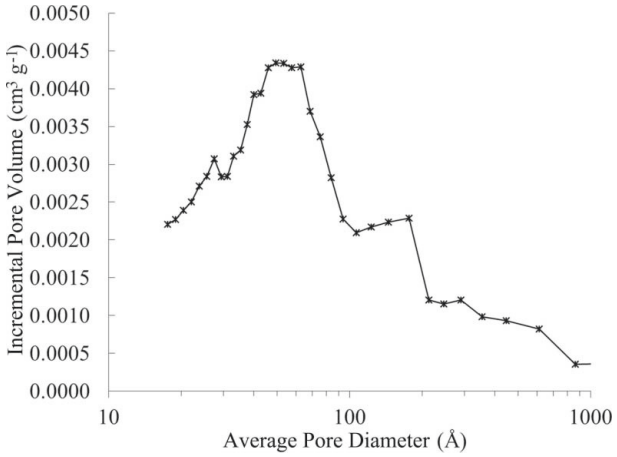

Figure 10
Pore size distribution in a 4 d-old S-activated slag paste, obtained using the adsorption branch from nitrogen sorption data.

S-activated metakaolin) and Fig. 8(*c*) (H- and S-activated slag). For H-activated metakaolin (Fig. 7*d*) the Porod slope for the different unified fits is relatively uncertain apart from immediately after initial mixing ($P = 3.95 \pm 0.05$) and fully cured (90 d, $P = 3.82 \pm 0.14$). The uncertainty for the high-Q-range fit (Level 2) is most likely attributable to the relatively small size of the Porod region together with the existence of an incoherent scattering background [Bk in equation (1)]. The low-Q-range Porod fit uncertainty is also probably due to the small size of the Porod region (existing between the two Guinier regions), but may in addition be influenced by the uncertainty associated with R_g for the Level 1 Guinier region. For S-activated metakaolin the Porod slope is well defined and remains relatively unchanged during the first 24 h of reaction ($P \simeq 3.9$). The relatively large error associated with the Level 1 Porod slope for this sample at 90 d is due to the emergence of a smaller-length-scale region (Level 2) which limits the Q range of the Porod region for Level 1. At 90 d, the Level 2 Porod region for S-activated metakaolin has a slope of 4.40 ± 0.15 (see Fig. S16 in the supporting information) (Schmidt *et al.*, 1991). However, it is likely that part of this increase in slope can be attributed to the incoherent scattering/background visible at high Q values (Fig. 4*c*) and therefore it is not indicative of a change in the surface roughness scattering. In general, the surface roughness scattering for metakaolin-based alkali-activated pastes is seen to be relatively smooth ($P > 3.8$).

The Porod regions for the slag-based alkali-activated pastes are displayed in Fig. 8(*c*). For S-activated slag there is no Level 2 Porod region owing to the extremely small R_g (~25 Å), which dominates the high-Q region of the SANS data. This is also the case for S-activated metakaolin, where no Level 2 Porod region is visible in the data (Fig. 7*f*). Hence, the Porod slope seen Fig. 8(*c*) for S-activated slag is associated with low-Q scattering. There is a slight decrease in the slope during the initial stages of reaction (4 h), from 3.53 ± 0.06 in slag powder to 3.37 ± 0.14. Although the error associated with the Porod slope at ~4 h is relatively large, this trend may be attributed to a slight increase in surface roughness of the partially dissolved slag particles during the initial stages of reaction.

3.5. Influence of particle morphology and activator chemistry on pore structure evolution

Two aspects of the pore structure of AAMs that are accessible using SANS are the average size of the nanoscale pores (as opposed to micrometre size) and the pore–solid interfacial roughness. In this investigation it is seen that the average pore size is dictated by the type of activator used (hydroxide *versus* silicate) and not by other variables such as precursor particle morphology or precursor chemistry. This is evident in Figs. 7(*a*)–7(*c*) and Figs. 8(*a*) and 8(*b*), where the S-activated pastes have much smaller pores compared to the H-activated pastes. However, the development of the small pores for S-activated metakaolin occurs much later after initial mixing when compared to S-activated slag (~18 h compared to ~3 h in slag). This delay in development of the small pores may be attributed to differences in paste chemistry, since slag is rich in calcium and therefore will form gel pores (~20–50 Å) associated with the C–(N)–A–S–H gel. On the other hand, metakaolin-based pastes do not contain any calcium, and therefore fewer gel pores tend to exist in the paste when fully cured (White, Provis, Proffen & van Deventer, 2010).

Another important aspect of the SANS data is the evolution of the pore size for H-activated systems. For metakaolin-based H-activated paste the pores with $R_g < 280$ Å are seen to increase in size as the reaction progresses. However, it is generally understood that the pore size tends to decrease as the reaction progresses, especially for the case of capillary pores (which are larger than gel pores) (Halperin *et al.*, 1994). Nevertheless, previous literature has reported an increase in size of small gel pores for the case of blended OPC–slag pastes with high slag content (Gorce & Milestone, 2007), which is also seen to occur here for the H-activated pastes (metakaolin and slag). This increase in gel pore size may also occur in the S-activated pastes, as visible by the increase in R_g sometime between ~20 h and 90 d for S-activated metakaolin. However, it may be possible that exposure to drying conditions for the 90 d sample (the sample was in powder form) may have altered the pore structure. Hence, SANS is well suited for analyzing *in situ* the evolution of the pore structure at the nanometre length scale (gel pores and small capillary pores) without the need to perform potentially damaging pretreatment methods such as drying. Further analysis is required to assess the changes that occur to the pastes during longer time scales (days to months) to obtain a complete understanding of the evolution of the nanosized pores in AAMs.

4. Conclusions

Here, the characteristic pore size at the nanoscale has been elucidated for a range of sodium-based AAMs during the initial stages of reaction using SANS analysis. Contrast matching experiments using H_2O/D_2O yield unexpected results for the AAM precursors (metakaolin and slag), especially for the case of metakaolin, where multiple contrast points were observed. However, in general, the contrast matching experiments revealed that the scattering measured using SANS is attributable to the pores in the precursor powders and the pastes, and therefore *in situ* measurements of the alkali-activation reaction reveal the changes occurring to the nanosized pores as the reaction progresses.

One of the main advantages of the SANS technique for investigating the nanosized pores in cement-based materials is that it is a nondestructive method and can be applied to pastes at any stage of the reaction. Hence, in this investigation we were able to measure the evolution of the pore structure during the initial stages of reaction (initial 24 h), revealing that the development of the nanosized pores is mostly dependent on the availability of free silica in the activator. For H-activated samples, the average pore size at the nanometre length scale is relatively large (small capillary pores or large gel pores), whereas for S-activated samples these pores are significantly smaller (gel pores). Furthermore, as the reaction

progresses over the initial 24 h, these nanosized pores are seen to increase in average size, especially for the H-activated pastes. The type of precursor influences the stage at which the gel pores develop in the S-activated pastes, since the availability of calcium in slag enables the faster development of gel pores during the initial stages of reaction in comparison to metakaolin-based pastes. The development of gel pores forming a percolated pore network in AAMs is closely linked to an increase in the long-term durability of these sustainable cements, and therefore S-activated slag pastes will be more durable than H-based slag pastes. Furthermore, given that a small number of gel pores may exist in S-activated metakaolin pastes, it may be possible to augment the chemistry of this AAM to increase the overall quantity of gel pores in this material and therefore develop durable metakaolin-based AAMs.

Acknowledgements

The authors would like to acknowledge the assistance of Anna Blyth in collecting the nitrogen sorption data. The participation of CEW and KP in this work was in part supported by Los Alamos National Laboratory, which is operated by Los Alamos National Security LLC under DOE contract DE-AC52-06NA25396. Furthermore, CEW gratefully acknowledges the support of the US Department of Energy through the LANL/LDRD Program and the National Science Foundation under grant No. 1362039. This research was performed on the LQD instrument at the Lujan Center at Los Alamos National Laboratory, supported by DOE-Basic Energy Sciences under FWP #2012LANLE389.

References

Allen, A. J., Thomas, J. J. & Jennings, H. M. (2007). *Nat. Mater.* **6**, 311–316.
Beaucage, G. (1995). *J. Appl. Cryst.* **28**, 717–728.
Beaucage, G. (1996). *J. Appl. Cryst.* **29**, 134–146.
Beaucage, G., Kammler, H. K. & Pratsinis, S. E. (2004). *J. Appl. Cryst.* **37**, 523–535.
Bell, J. L., Driemeyer, P. E. & Kriven, W. M. (2009*a*). *J. Am. Ceram. Soc.* **92**, 1–8.
Bell, J. L., Driemeyer, P. E. & Kriven, W. M. (2009*b*). *J. Am. Ceram. Soc.* **92**, 607–615.
Bell, J. L., Sarin, P., Driemeyer, P. E., Haggerty, R. P., Chupas, P. J. & Kriven, W. M. (2008). *J. Mater. Chem.* **18**, 5974–5981.
Bell, J. L., Sarin, P., Provis, J. L., Haggerty, R. P., Driemeyer, P. E., Chupas, P. J., van Deventer, J. S. J. & Kriven, W. M. (2008). *Chem. Mater.* **20**, 4768–4776.
Blackford, M. G., Hanna, J. V., Pike, K. J., Vance, E. R. & Perera, D. S. (2007). *J. Am. Ceram. Soc.* **90**, 1193–1199.
Brough, A. R. & Atkinson, A. (2002). *Cem. Concr. Res.* **32**, 865–879.
Chen-Tan, N. W., van Riessen, A., Ly, C. V. & Southam, D. C. (2009). *J. Am. Ceram. Soc.* **92**, 881–887.
Deventer, J. S. J. van, Provis, J. L. & Duxson, P. (2012). *Miner. Eng.* **29**, 89–104.
Duxson, P., Lukey, G. C. & van Deventer, J. S. J. (2006). *J. Non-Cryst. Solids*, **352**, 5541–5555.
Duxson, P., Lukey, G. C. & van Deventer, J. S. J. (2007). *J. Non-Cryst. Solids*, **353**, 2186–2200.
Duxson, P. & Provis, J. L. (2008). *J. Am. Ceram. Soc.* **91**, 3864–3869.
Duxson, P., Provis, J. L., Lukey, G. C., Mallicoat, S. W., Kriven, W. M. & van Deventer, J. S. J. (2005). *Colloids Surf. A Pysicochem. Eng. Asp.* **269**, 47–58.
Duxson, P., Provis, J. L., Lukey, G. C. & van Deventer, J. S. J. (2007). *Cem. Concr. Res.* **37**, 1590–1597.
Duxson, P., Provis, J. L., Lukey, G. C., van Deventer, J. S. J., Separovic, F. & Gan, Z. H. (2006). *Ind. Eng. Chem. Res.* **45**, 9208–9210.
Duxson, P., Provis, J. L., Lukey, G. C., Separovic, F. & van Deventer, J. S. J. (2005). *Langmuir*, **21**, 3028–3036.
Fernández-Jiménez, A. & Palomo, A. (2007). *Mater. Constr.* **57**, 7–22.
Fernández-Jiménez, A., Palomo, A. & Criado, M. (2005). *Cem. Concr. Res.* **35**, 1204–1209.
Fernández-Jiménez, A. M., Palomo, A. & López-Hombrados, C. (2006). *ACI Mater. J.* **103**, 106–112.
Gorce, J.-P. & Milestone, N. B. (2007). *Cem. Concr. Res.* **37**, 310–318.
Gordon, M., Bell, J. L. & Kriven, W. M. (2005). *Ceram. Trans.* **165**, 95–106.
Halperin, W. P., Jehng, J.-Y. & Song, Y.-Q. (1994). *Magn. Reson. Imaging*, **12**, 169–173.
Hjelm, R. P. (1988). *J. Appl. Cryst.* **21**, 618–628.
Ilavsky, J. & Jemian, P. R. (2009). *J. Appl. Cryst.* **42**, 347–353.
Jennings, H. M., Bullard, J. W., Thomas, J. J., Andrade, J. E., Chen, J. J. & Scherer, G. W. (2008). *J. Adv. Concr. Technol.* **6**, 5–29.
Lloyd, R. R., Provis, J. L. & van Deventer, J. S. J. (2009*a*). *J. Mater. Sci.* **44**, 608–619.
Lloyd, R. R., Provis, J. L. & van Deventer, J. S. J. (2009*b*). *J. Mater. Sci.* **44**, 620–631.
Maitland, C. F., Buckley, C. E., O'Connor, B. H., Butler, P. D. & Hart, R. D. (2011). *J. Appl. Cryst.* **44**, 697–707.
Mang, J. T. & Hjelm, R. P. (2013). *Propellants Explosives Pyrotech.* **38**, 831–840.
Mang, J. T., Hjelm, R. P., Orler, E. B. & Wrobleski, D. A. (2008). *Macromolecules*, **41**, 4358–4370.
Mang, J. T., Skidmore, C. B., Hjelm, R. P. & Howe, P. M. (2000). *J. Mater. Res.* **15**, 1199–1208.
Mazumder, S. & Sequeira, A. (1992). *Pramana J. Physics* **38**, 95–159.
Meral, C., Benmore, C. J. & Monteiro, P. J. M. (2011). *Cem. Concr. Res.* **41**, 696–710.
Myers, R. J., Bernal, S. A., San Nicolas, R. & Provis, J. L. (2013). *Langmuir*, **29**, 5294–5306.
Palomo, A., Banfill, P. F. G., Fernández-Jiménez, A. & Swift, D. S. (2005). *Adv. Cem. Res.* **17**, 143–151.
Phair, J. W., Schulz, J. C., Bertram, W. & Aldridge, L. P. (2003). *Cem. Concr. Res.* **33**, 1811–1824.
Potton, J. A., Daniell, G. J. & Rainford, B. D. (1988). *J. Appl. Cryst.* **21**, 663–668.
Provis, J. L. & van Deventer, J. S. J. (2007). *Chem. Eng. Sci.* **62**, 2309–2317.
Provis, J. L., Duxson, P., Lukey, G. C. & van Deventer, J. S. J. (2005). *Chem. Mater.* **17**, 2976–2986.
Pruett, R. J. & Webb, H. L. (1993). *Clays Clay Miner.* **41**, 514–519.
Rahier, H., Wastiels, J., Biesemans, M., Willlem, R., Van Assche, G. & Van Mele, B. (2007). *J. Mater. Sci.* **42**, 2982–2996.
Rees, C. A., Provis, J. L., Lukey, G. C. & van Deventer, J. S. J. (2007*a*). *Langmuir*, **23**, 8170–8179.
Rees, C. A., Provis, J. L., Lukey, G. C. & van Deventer, J. S. J. (2007*b*). *Langmuir*, **23**, 9076–9082.
Richardson, I. G., Brough, A. R., Groves, G. W. & Dobson, C. M. (1994). *Cem. Concr. Res.* **24**, 813–829.
Scherer, G. W. (2012). *J. Chin. Ceram. Soc.* **40**, 1071–1080.
Scherer, G. W., Valenza, J. J. & Simmons, G. (2007). *Cem. Concr. Res.* **37**, 386–397.
Schmidt, P. W., Avnir, D., Levy, D., Höhr, A., Steiner, M. & Röll, A. (1991). *J. Chem. Phys.* **94**, 1474–1479.
Seeger, P. A. & Hjelm, R. P. (1991). *J. Appl. Cryst.* **24**, 467–478.
Shi, C., Krivenko, P. V. & Roy, D. M. (2006). *Alkali-Activated Cements and Concretes.* New York: Taylor and Francis.
Singh, P. S., Bastow, T. & Trigg, M. (2005). *J. Mater. Sci.* **40**, 3951–3961.

Singh, P. S., Trigg, M., Burgar, I. & Bastow, T. (2005). *Mater. Sci. Eng. A*, **396**, 392–402.
Steins, P., Poulesquen, A., Diat, O. & Frizon, F. (2012). *Langmuir*, **28**, 8502–8510.
Steins, P., Poulesquen, A., Frizon, F., Diat, O., Jestin, J., Causse, J., Lambertin, D. & Rossignol, S. (2014). *J. Appl. Cryst.* **47**, 316–324.
Steveson, M. & Sagoe-Crentsil, K. (2005). *J. Mater. Sci.* **40**, 4247–4259.
Temuujin, J., Rickard, W., Lee, M. & van Riessen, A. (2011). *J. Non-Cryst. Solids*, **357**, 1399–1404.
Thomas, J. J., Allen, A. J. & Jennings, H. M. (2012). *Cem. Concr. Res.* **42**, 377–383.
Thomas, J. J. & Jennings, H. M. (1999). *Chem. Mater.* **11**, 1907–1914.
Valenza, J. J. II & Thomas, J. J. (2012). *Cem. Concr. Res.* **42**, 440–446.
White, C. E. (2012). *Z. Kristallogr.* **227**, 304–312.
White, C. E., Provis, J. L., Bloomer, B., Henson, N. J. & Page, K. (2013). *Phys. Chem. Chem. Phys.* **15**, 8573–8582.
White, C. E., Provis, J. L., Llobet, A., Proffen, T. & van Deventer, J. S. J. (2011). *J. Am. Ceram. Soc.* **94**, 3532–3539.
White, C. E., Provis, J. L., Proffen, T. & van Deventer, J. S. J. (2010). *J. Am. Ceram. Soc.* **93**, 3486–3492.
White, C. E., Provis, J. L., Proffen, T. & van Deventer, J. S. J. (2012). *AIChE J.* **58**, 2241–2253.
White, C. E., Provis, J. L., Proffen, T., Riley, D. P. & van Deventer, J. S. J. (2010*a*). *J. Phys. Chem. A*, **114**, 4988–4996.
White, C. E., Provis, J. L., Proffen, T., Riley, D. P. & van Deventer, J. S. J. (2010*b*). *Phys. Chem. Chem. Phys.* **12**, 3239–3245.
Williams, R. P., Hart, R. D. & van Riessen, A. (2011). *J. Am. Ceram. Soc.* **94**, 2663–2670.
Zhang, Z., Wang, H., Provis, J. L., Bullen, F., Reid, A. & Zhu, Y. (2012). *Thermochim. Acta*, **539**, 23–33.